25th ABCM International Congress of Mechanical Engineering
October 20-25, 2019, Uberlândia, MG, Brazil

COB-2019-0632
NUMERICAL SIMULATION OF A SOLAR PHOTO-THERMOCHEMICAL REACTOR FOR THE PRODUCTION OF SYNGAS USING THE SOLAR DRIVEN CO_2 REFORMING OF METHANE

André Adriano da Silva Cruz
Jornandes Dias da Silva
Polytechnic School - UPE, Laboratory of Environmental and Energetic Technology; Rua Benfica - 455, Madalena, Recife – PE, Brazil, Cep: 50750-470
andre.adriano@ymail.com
jornandesdias@poli.br

Abstract. *This work shows a gas-solid pseudo-homogeneous model to simulate the governing equations of mass and heat transfers coupled with thermochemical kinetic model in photo-thermochemical reactor with radiative heat loss. High temperature heat transfer, mass transfer, and thermochemical storage performances of the solar driven CO_2 reforming of methane are numerically investigated. The computational simulation of nonlinear partial differential equations (NLPDEs) has been one of the most difficult challenges for researchers worldwide because of the numerical stability requirement of the results. The developed model is described by a system of Partial Differential Equations (PDEs). The system of original EDPs is transformed into simpler system of Ordinary Differential Equations (ODEs) using the Coupled Integral Equation Approach (CIEA). Thus, the temperature profile at the surface of the solid phase and the temperature profile in the gas phase are obtained. In addition, the conversions of reactants of CH_4 and CO_2 are studied under different operating temperatures.*

Keywords: *Mathematical Model, Reforming of CO_2, Solar Energy, Photo-thermochemical, Hydrogen*

1. INTRODUCTION

The worldwide's renewable energy is widely dominated by the burning of fossil fuels which leads to the emissions of CO_2 into the atmosphere and is known to contribute to the undesired global warming. The questions of fossil fuel depletion and climate change have resulted in development of solar industrial process solutions. Reforming processes which make use of solar heat to drive high temperature endothermic chemical reactions are known as solar photo-thermochemical processes. Solar photo-thermochemical reforming is based in the use of concentrated solar energy as a heating source of high temperature for conducting an endothermic chemical transformation (Villafán-Vidales et al., 2017; Anjos et al., 2019). The solar reforming technology can be used to produce renewable energies (as solar hydrogen production) as from solar photo-thermochemical reaction systems (STRSs). Actually, hydrogen (H_2) has a long tradition as an energy carrier and as an important raw material in chemical industries and refineries (Cruz and Silva, 2017; Silva and Abreu, 2016). Theoretically, all hydrogen produced today is sourced from fossil fuels using the steam reforming of methane as principal process. Hydrogen (H_2) production from steam reforming process of light hydrocarbon is a worldwide need nowadays (Abdesslem et al., 2013).

Solar driven carbon dioxide (CO_2) reforming of methane (SDCDRM) can be considered as a promising process for producing solar hydrogen (H_2). The SDCDRM is based on the utilization of concentrated solar irradiation (CSI) as an energy source to maintain high operating temperature. Accordingly, it was defined the concept of solar photo-thermochemical reactor (SPR) to study the SPR process. SPR is an important and valuable device for process intensification where many applications can be carried out at high operating temperature. When compared with conventional reactors, SPR reports several advantages, such as high surface-to-volume ratio and excellent mass and heat transfer performances (Chen et al., 2018; Jin et al., 2018). This SPR model became an efficient laboratory device for processing heterogeneously catalyzed gaseous reactions.

The modelling of SPR is still an open issue, thus the topic is a very actual subject for renewable energy engineering. In this context, fluid-solid pseudo-homogeneous (FSPH) models are often used to model the heterogeneous catalytic systems taking into account the effects of intraparticle processes only by means of effectiveness factors (Anjos et al., 2017; Silva et al., 2019; Matienzo, 2018). The FSPH models are widely used to model heterogeneous systems since these models handle all processes occurring simultaneously in the fluid phase.

In this work, a mathematical model has been developed to investigate the heat and mass transfer phenomena coupled with thermochemical reaction kinetics in SPR. The performance from SPR using the SDCDRM process is numerically

investigated in terms of the temperature profiles in the gaseous and solid phases. On the other hand, it was also studied the production H_2 as well as conversions of CH_4 and CO_2 in SPR.

2. SOLAR THERMOCHEMICAL MODELLING

2.1 Problem description

In the last two decades, Researches have proven the efficient use of solar thermal energy for driving highly endothermic reforming reactions. For this purpose, a schematic setup (see Fig. 1) was employed to study the SDCDRM process in STR.

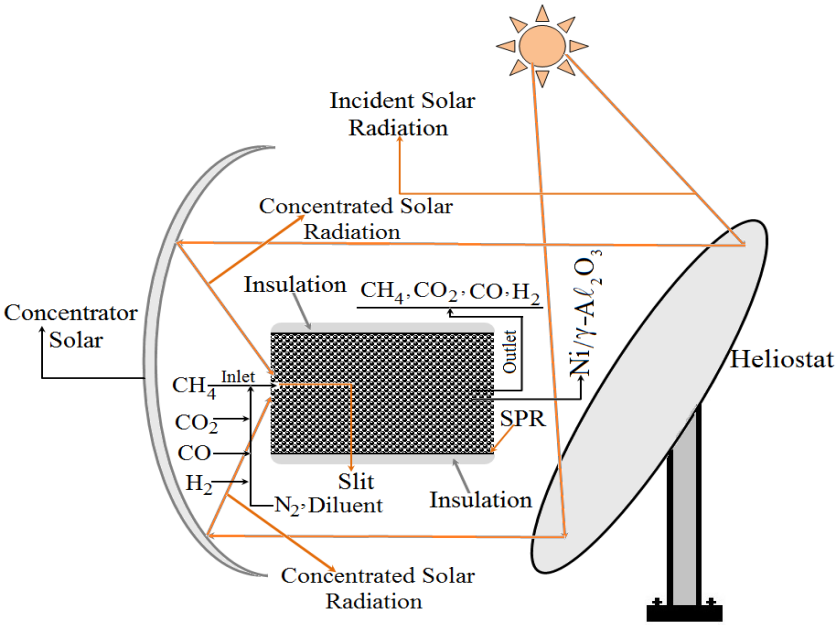

Figure 1. Schematic setup from SPR

2.2 Kinetic mechanism

The reforming reaction of CO_2 is essential to produce H_2 and syngas (H_2 e CO) which are highly endothermic. The SDCDRM process has a limited equilibrium and comprises one reforming reaction as follows.

$$CH_4 + CO_2 \rightarrow 2CO + 2H_2 \; ; \; \Delta H^0_{298K} = +247\, kJ / mol \tag{1}$$

The component models of these reactions are defined as toluene (CH_4), carbon dioxide (CO_2), carbon and monoxide (CO), hydrogen (H_2).

2.3 Kinetic model

The overall rate equation of the reaction, Eq. (1), is based on the Langmuir-Hinshelwood kinetic model and it can be found in Chen et al., (2018) as follows.

$$R_{SDCDRM} = \frac{k_{SDCDRM}\, K_{CH_4} K_{CO_2} P_{CH_4} P_{CO_2}}{\left(1 + K_{CH_4} P_{CH_4} + K_{CO_2} P_{CO_2}\right)^2} \tag{2}$$

In Eq. (2), R_{SDCDRM} (kmol/$kg_{cat.}$h) is the kinetic rate from SDCDRM reaction; k_{SDCDRM} (kmol/ $kg_{cat.}$h) is the kinetic rate constant from SDCDRM reaction, K_{CH4} is the surface adsorption equilibrium constant of CH_4, K_{CO2} (kPa^{-1}) is the surface adsorption equilibrium constant of CO_2, P_{CH4} (kPa) is the partial pressure of CH_4, P_{CO2} (kPa) is the partial pressure of CO_2, respectively.

The net rates of each chemical components (r_i, i = CH_4, CO_2, CO and H_2) are computed in Tab. 1 and can be found in Reference (Cruz and Silva, 2017).

Table 1. Net rates of components i from Eq. (1).

Components	Equations of net rates	Components	Equations of net rates
CH_4	$r_{CH_4} = -\eta_1 R_{SDCDRM}$	CO	$r_{CO} = +\eta_1 R_{SDCDRM}$
CO_2	$r_{CO_2} = -\eta_1 R_{SDCDRM}$	H_2	$r_{H_2} = +\eta_1 R_{SDCDRM}$

2.4 SPR modelling

A theoretical dynamic equation is developed to describe the heat transfer process of the gas phase on directly irradiated gas-solid SPR. The developed equation provides clear information to conduct the temperature distribution of the gas phase in porous medium reactive packed bed. Thus, the governing energy balance of the gas phase in porous medium SPR is built as follows.

- Energy balance in the gas phase;

$$\sum_{i=1}^{4} \rho_{g,i} C_{p,g,i} \left(\frac{\partial T_g}{\partial t} + \frac{4 q_g}{\pi d_\mu^2} \frac{\partial T_g}{\partial z} \right) = \lambda_{g,eff} \frac{\partial^2 T_g}{\partial z^2} - h_{gs} \frac{\left(1-\varepsilon_b\right)}{\varepsilon_b} \frac{6}{d_p} \left(T_g - T_s \right); 0 \le z \le L_z, t > 0 \tag{3}$$

In Equation (3), $C_{p,g}$ (kJ/kg K) is the molar heat capacity at constant pressure of the gas mixture, T_g (K) is the gas temperature, z (m) is the axial direction, respectively; $\lambda_{g,eff}$ (W/m K) is the effective thermal conductivity of the gas phase, h_{gs} (W/m^2 K) is the gas-solid heat transfer coefficient, d_p (m) is the diameter of the solid particles, T_s (K) is the solid temperature, respectively.

The suitable initial and boundary conditions from Eq. (3) are given as follows.

$$T_g\Big|_{t=0,\,0\le z\le L_z} = 0 \; ; \; \lambda_{g,eff} \frac{\partial T_g}{\partial z}\bigg|_{z=0^+,\,t\ge 0} = \rho_g C_{p,g} \frac{4 q_g}{\pi d_\mu^2} \left(T_g\Big|_{z=0^+,\,t\ge 0} - T_{g,in} \right); \frac{\partial T_g}{\partial z}\bigg|_{z=L_z,\,t\ge 0} = 0 \tag{4}$$

The reactive packed bed consists of a particle network structure with porosity typically of about 40-60%. The tortuous structure of sphere particles could also give rise some turbulence with a concomitant increase in heat transfer between the solid and fluid phases. The thermal storage takes place on the solid particles to ensure sufficient energy for processing the endothermic reactions from the SDCDRM process. In the presence of radiation, the energy balance equation for temperature at the surface of the solid phase is given as follows.

- Energy balance at the surface of the solid phase;

$$\sum_{i=1}^{4} \rho_{s,i} C_{p,s,i} \frac{\partial T_s}{\partial t} = \left(\lambda_{s,eff} = \lambda_s \left(T_{g,0} \right) + \frac{16 n^2 \sigma T_\infty^3}{3 k_R} \right) \frac{\partial^2 T_s}{\partial z^2} + \rho_s \frac{\left(1-\varepsilon_p\right)}{\varepsilon_p} \Delta H_1 \eta_1 R_1 + h_{gs} \frac{6}{d_p} \frac{\left(1-\varepsilon_b\right)}{\varepsilon_b} \left(T_g - T_s \right) - \varepsilon_w A_{cs} \sigma \left(T_s^4 - T_\infty^4 \right); 0 \le z \le L_z, t > 0 \tag{5}$$

In Eq. (5), ρ_s (kg/m^3) is the density of the solid phase, $C_{p,s}$ (kJ/kg K) is the molar heat capacity at constant pressure of the solid phase, λ_s (W/m K) is the solid thermal conductivity, $q_{irrad.}$ (W/m^2) is the irradiative heat flux, ε_p (m^{3}gas/m^{3}reactor) is the void fraction of the solid phase, ΔH_j (kJ/kmol) is the heat of reaction, η_1 (-) is the effectiveness factor, R_j (kmol/kg$_{cat.}$ h) is the overall rate of reaction j, ε_w (-) is the emissivity of wall, A_{cs} (m^2) is the cross-cut section area, σ (W/m^2 T^4) is the Stefan-Boltzmann constant, and T_∞ (K) is the ambient temperature, respectively.

The suitable initial and boundary conditions from Eq. (5) are given as follows.

$$T_s\big|_{t=0,0\le z\le L_z} = 0\ ;\ -\lambda_s\left(T_g,0\right)\left.\frac{\partial T_s}{\partial z}\right|_{z=0^+,t\ge 0} = \frac{DNI}{L_z};\ \left.\frac{\partial T_s}{\partial z}\right|_{z=L_z,t\ge 0} = 0 \tag{6}$$

The mass balance equations are presented for each component i (i = CH_4, CO_2, CO and H_2) in SPR. A PHM model is developed to report every chemical component i in detail. In this model, it is assumed that the gas properties and flow at the inlet cross-section of the reactor are uniform. Thus, the mass balance equation of chemical components i in SPR is given as follows.

$$\varepsilon_b\frac{\partial C_i}{\partial t}+\frac{4q_g}{\pi d_\mu^2}\frac{\partial C_i}{\partial z} = \varepsilon_b D_{ax,i}\frac{\partial^2 C_i}{\partial z^2} + \rho_s\eta_1\sum_{i=1}^{4} r_i\ ;\ 0\le z\le L_z, t>0 \tag{7}$$

In Eq. (7), C_i (mol/m^3) is the concentration of components i at the surface of catalyst particles, Q_g (m^3/min) is the gas flow rate, d_μ (m) is the inner diameter from SPR, $D_{ax,i}$ (m^2/min) is the axial mass dispersion coefficient of components i, r_i (kmol/kg$_{cat.}$ min) is the net rates from components i, respectively.

The suitable initial and boundary conditions from Eq. (7) are presented as follows.

$$\begin{aligned} &C_i\big|_{t=0,0\le z\le L_z} = 0; \varepsilon_b D_{ax,i}\left.\frac{\partial C_i}{\partial z}\right|_{z=0^+,t\ge 0} = \frac{4q_g}{\pi d_\mu^2}\left[C_i\big|_{z=0^+,t\ge 0} - C_{i,in}\right]; \\ &D_{ax,i}\left.\frac{\partial C_i}{\partial z}\right|_{z=L_z,t\ge 0} = k_{g,i,eff}\left(C_\infty - C_i\big|_{z=L_z,t\ge 0}\right) \end{aligned} \tag{8}$$

3. NUMERICAL SOLUTION OF THE MATHEMATICAL MODELLING

3.1 Hermite approximation

The basic concept for the coupled integral equations approach (CIEA) is the Hermite approximation which can be given by a general equation as follows.

$$\int_{x_{i-1}}^{x_i} f(x)dx = \sum_{\nu=0}^{\alpha} c_\nu(\alpha,\beta) h_i^{\nu+1} f^{(\nu)}\left(x_{i-1}\right) + \sum_{\nu=0}^{\beta} c_\nu(\beta,\alpha)(-1)^\nu h_i^{\nu+1} f^{(\nu)}\left(x_i\right) + E_{\alpha,\beta} \tag{9}$$

Where,

$$h_i = x_i - x_{i-1},\ c_\nu(\alpha,\beta) = \frac{(\alpha+1)!(\alpha+\beta-\nu+1)!}{(\nu+1)!(\alpha-\nu)!(\alpha+\beta+2)!} \tag{10}$$

The function (f(x)) and its derivatives $f^{(\nu)}(x)$ are reported for all $x \in [x_{i-1}, x_i]$. $E_{\alpha,\beta}$ is defined as the error in the approximation. In this context, it has been assumed that $f^{(\nu)}(x_{i-1}) = f_i^{(\nu)}$ for $\nu = 0, 1, 2, 3,\ldots, \alpha$ and $f^{(\nu)}(x_i) = f_i^{(\nu}$ for $\nu = 0, 1, 2, 3,\ldots, \beta$. As result, this integration formula can give different levels of approximation that are traditionally called of $H_{\alpha,\beta}$. Thus, approximations of order higher than $H_{1,1}$ involve derivatives of order higher than one. These derivatives are avoided for the sake of simplicity of the methodology. Here, it was considered only two different approximations as follows.

$$H_{0,0} \to \int_0^h f(x)dx \approx \frac{1}{2}h\left[f(x)\big|_{x=0} + f(x)\big|_{x=h}\right] \tag{11}$$

$$H_{1,1} \to \int_0^h f(x)dx \approx \frac{1}{2}h\left[f(0)+f(h)\right] + \frac{1}{12}h^2\left[\left.\frac{df(x)}{dx}\right|_{x=0} - \left.\frac{df(x)}{dx}\right|_{x=h}\right] \tag{12}$$

In Eqs. (11) and (12), $H_{0,0}$ is the trapezoidal integration rule, $H_{1,1}$ is the corrected trapezoidal integration rule, respectively.

3.2 Application of the CIEA methodology

For solving the equations system, i.e., Eqs. (3)-(8) were resolved using the CIEA methodology. This methodology is used to transform EDPs into EDOs taking into account the boundary conditions. Here, it was used the expressions below to transform EDPs into EDOs in together with the boundary conditions.

$$\bar{f}_j(t) = \frac{1}{L_z}\int_0^{L_z} f_j(z,t)dz;\ j = g,s\ and\ i \tag{13}$$

$$f_j(L_z,t) - f_j(0,t) \cong \frac{L_z}{2}\left[\left.\frac{\partial f_j(z,t)}{\partial z}\right|_{z=0} + \left.\frac{\partial f_j(z,t)}{\partial z}\right|_{z=L_z}\right];\ j = g,s\ and\ i \tag{14}$$

$$\bar{f}_j(t) \cong \frac{L_z}{2}\left[f_j(0,t) + f_j(L_z,t)\right] + \frac{L_z^2}{12}\left[\left.\frac{\partial f_j(z,t)}{\partial z}\right|_{z=0} - \left.\frac{\partial f_j(z,t)}{\partial z}\right|_{z=L_z}\right];\ j = g,s\ and\ i \tag{15}$$

It is possible to transform the equations system, Eqs. (3)-(8), applying Eqs. (13)-(15) using the boundary conditions of each EDP. Thus, transformed equations are reported as follows.

- The transformed equation of the energy balance of the gas phase;

$$\frac{d\bar{T}_g(t)}{dt} = \alpha_{g,7}\bar{T}_g(t) + \alpha_{g,8}\bar{T}_s(t) + \alpha_{g,9}T_{g,in.} \tag{16}$$

- The transformed equation of the energy balance of the solid phase;

$$\frac{d\bar{T}_s(t)}{dt} = -\beta_{s,1}\bar{T}_s(t) + \beta_{s,1}\bar{T}_g(t) - \beta_{s,2}\bar{T}_s^4(t) + \beta_{s,2}T_{s,\infty}^4 + \beta_3\bar{R}_1(t) + \beta_4 \tag{17}$$

- The transformed equation of the mass balance equation of chemical components i;

$$\frac{d\bar{C}_i(t)}{dt} = \gamma_{14}\bar{C}_i(t) + \frac{\rho_s\eta_1}{\varepsilon_b}\sum_{i=1}^{4}\bar{r}_i(t) + \gamma_{15};\ i = CH_4, CO_2, CO, H_2 \tag{18}$$

All coefficients from Eqs. (16)-(18) are presented in Annexes A, B and C, respectively.

3.3 Approximation of the full solution

In order to solve the governing equations of the engineering problems, several numerical methods have been developed to solve EDPs. The choice of method is dependent on the desired accuracy as well as concerns about the stability and robustness of the system while maintaining computational efficiency. With respect to the transformed equations, Eq. (16)-(18), they are solved by Runge-Kutta Gill method. On the other hand, the full solution is approximated using Eqs. (19)-(21) as follows.

- The approximated solution of the energy balance of the gas phase;

$$T_g(z,t) = \frac{1}{2}T_g(z,t)\Big|_{t=0} + \sum_{k=1}^{\infty}\bar{T}_g(t)\sin\left(\frac{k\pi z}{L_z}\right) \tag{19}$$

- The approximated solution of the energy balance of the solid phase;

$$T_s(z,t) = \frac{1}{2}T_s(z,t)\Big|_{t=0} + \sum_{k=1}^{\infty}\bar{T}_s(t)\sin\left(\frac{k\pi z}{L_z}\right) \tag{20}$$

- The approximated solution of the mass balance equation of chemical components i;

$$C_i(z,t) = \frac{1}{2} C_i(z,t)\Big|_{t=0} + \sum_{k=1}^{\infty} \bar{C}_i(t) \sin\left(\frac{k\pi z}{L_z}\right); i = CH_4, CO_2, CO, H_2 \quad (21)$$

4. RESULTS AND DISCUSSIONS

4.1 Model parameters for simulations

A mathematical model has been used to investigate the performance from the SPR using the thermochemical energy of the reforming reaction (Eq. (1)). In Section 2, a full model is developed for simulating the heat and mass transfer processes coupled with thermochemical reaction kinetic in the SPR. A computational algorithm using the FORTRAN 95 was elaborated by the authors to solve the model equations mentioned in this work. The parameter values used to feed the computational algorithm are shown in Tab. 2 below.

Table 2. Reference parameters of the kinetic Modelling of the SDCDRM process in SPR.

Feed parameters	Values	References
k_{SDCDRM} (kmol/ $kg_{cat.}$sec.)	5.775×10^{5}	Chein et al., (2017)
K_{CH4} (kPa^{-1})	2.4317×10^{-6}	Chein et al., (2017)
K_{CO2} (kPa^{-1})	3.9008×10^{-5}	Chein et al., (2017)
P_{CH4} (kPa)	5.5664	Cruz and Silva, (2017)
P_{CO2} (kPa)	4.8471	Cruz and Silva, (2017)
$T_{g,0}$ (K)	300	Estimated
$T_{s,0}$ (K)	2000	Estimated
dμ (mm)	2.00	Estimated
d_p (mm)	0.10	Estimated
L_z (mm)	20.00	Estimated
q_g ($m^3 sec^{-1}$)	(2.536-5497) x 10^{-6}	Estimated
$P_{op.}$ (kPa)	650	Estimated
ε_b (m^3 gas/m^3 reactor)	0.41	Silva et al., (2019)
$\lambda_{g,eff.}$ (W/m K)	107.383	Chen et al., (2018)
h_{gs} ($Wm^{-2} K^{-1}$)	1.9561	Chen et al., (2018)
$C_{p,g}$ ($J\ kg^{-1}K^{-1}$)	35.00	Chen et al., (2018)
ρ_g ($kg\ m^{-3}$)	0.3857	Cruz and Silva, (2017)
ρ_s ($kg\ m^{-3}$)	3200	Cruz and Silva, (2017)
$C_{p,s}$ ($J\ kg^{-1}K^{-1}$)	336	Silva and Abreu, (2016)
$\lambda_{s,}(T_{g,0})$ (W/m K)	126.115	Chen et al., (2018)
n (-)	1.00	Chen et al., (2018)
σ ($W\ m^{-2}\ T^{-4}$)	2.67×10^{-8}	Chen et al., (2018)
k_R (m^{-1})	1.738×10^{4}	Chen et al., (2018)
ε_p (m^3 gas/m^3 reactor)	0.47	Silva et al., (2019)
$(\Delta H_1)^{SDCDRM}$ ($kJ/kmol^{-1}$)	293.872	Cruz and Silva, (2017)
η_1 (-)	0.0219	Cruz and Silva, (2017)
ε_w (-)	0.92	Abdesslem et al., (2013)
A_{cs} (m^2)	279	Abdesslem et al., (2013)
T_∞ (K)	300	Estimated
$D_{ax,\ CH4}$ (m^2/sec.)	9.32×10^{-6}	Cruz and Silva, (2017)
$D_{ax,\ CO2}$ (m^2/sec.)	4.95×10^{-6}	Cruz and Silva, (2017)
$D_{ax,\ CO}$ (m^2/sec.)	1.13×10^{-5}	Cruz and Silva, (2017)
$D_{ax,\ H2}$ (m^2/sec.)	8.21×10^{-6}	Cruz and Silva, (2017)
$k_{g,\ CH4,\ eff.}$ (m/sec.)	0.289	Silva et al., (2019)
$k_{g,\ CO2,\ eff.}$ (m/sec.)	0.697	Silva et al., (2019)
$k_{g,\ CO,\ eff.}$ (m/sec.)	0.379	Silva et al., (2019)
$k_{g,\ H2,\ eff.}$ (m/sec.)	0.134	Silva et al., (2019)
C_∞ (kg/m^3)	0.00	Estimated

Figure 2a reports the temperature profile at the surface of the solid phase and the temperature profile of the gas phase along SPR length, respectively. As shown in Fig. 2a, the temperature profile at the surface of the solid phase decreases from 2000K to more or less 1123K whereas the temperature profile of the gas phase increases from 300K to more or less 1123K. The temperature profiles of the solid and gas phases reach the same temperature at more or less 3.25 mm from SPR length (see Fig. 2a´. As from 3.25 mm, two-phase temperatures of 1123K were kept constant up to the ultimate length from SPR. Thus, the temperature of 1123K can be used as the optimum operating temperature.

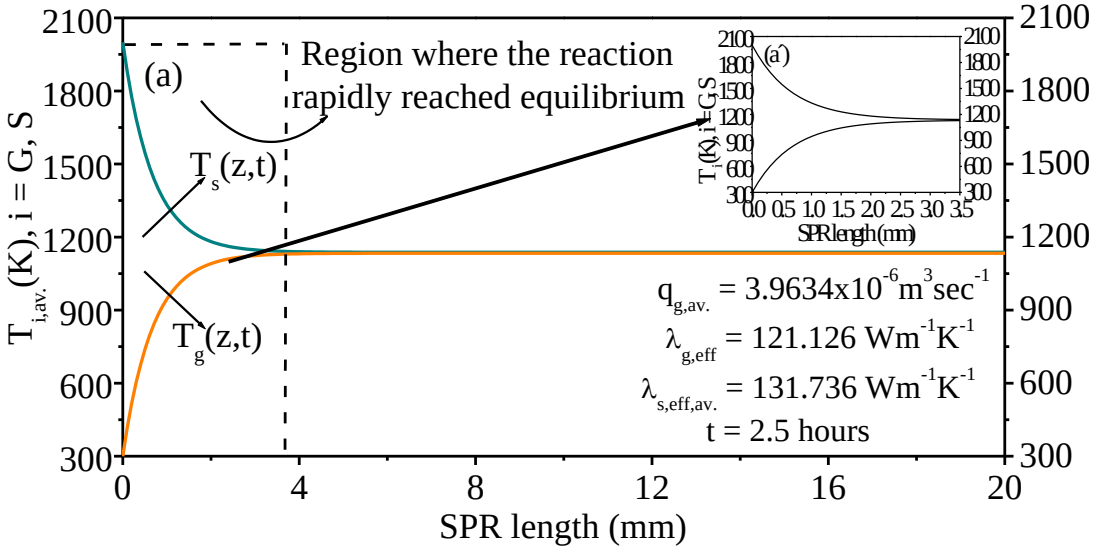

Figure 2. Average temperature profile at the surface of the solid phase and average temperature profile of the gas phase.

Figure 3 describes the average temperature profile at the surface of the solid phase and the average temperature profile of the gas phase along the SPR length, respectively. As shown in Fig. 3, the average temperature profile at the surface of the solid phase decreases from 2000K according to the DNI decreases. On the other hand, the average temperature profile of the gas phase increases as the DNI increases. The average temperature profiles of the solid and gas phases reach the same temperature at more or less 3.25 mm from SPR length. As from 3.25 mm, two-phase temperatures of 1185K were kept constant up to the ultimate length from SPR.

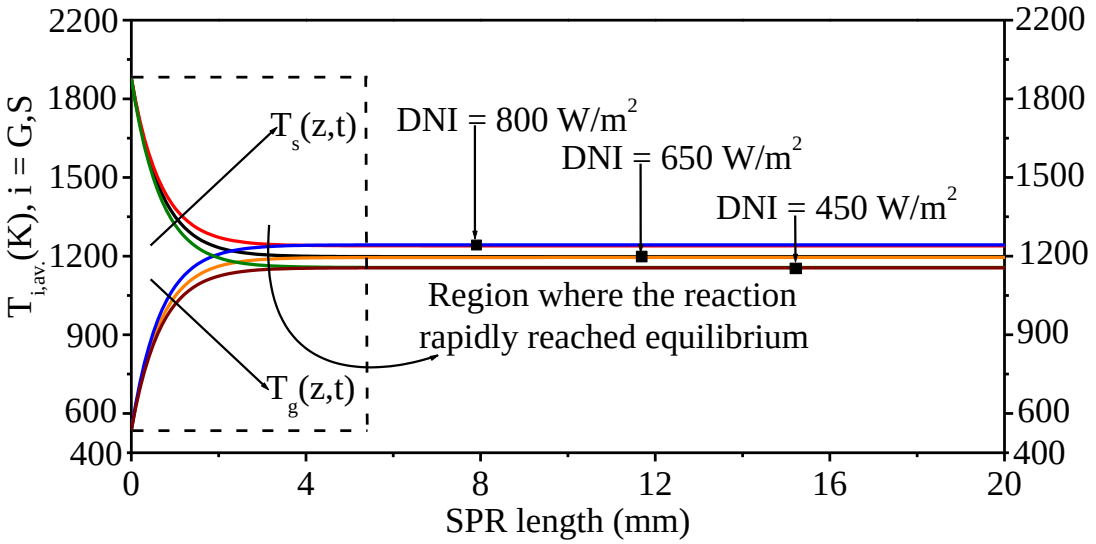

Figure 3. Average temperature profile at the surface of the solid phase and the average temperature profile of the gas phase at three different DNI.

In order to investigate the effect of the $\lambda_{s,eff}$ on production of H_2, Fig. 4 presents this product with its respective gradual effects along the packed bed from porous medium SPR with radiative heat loss. From Figure 4, it is observed that the mole concentration of H_2 increases sharply at the near gas inlet surface region and then higher H_2 values are

reached in upper values of the $\lambda_{s,eff}$. At the gas outlet surface region, it was reported that the mole concentration of H_2 is gradually increasing with the increase of the $\lambda_{s,eff}$.

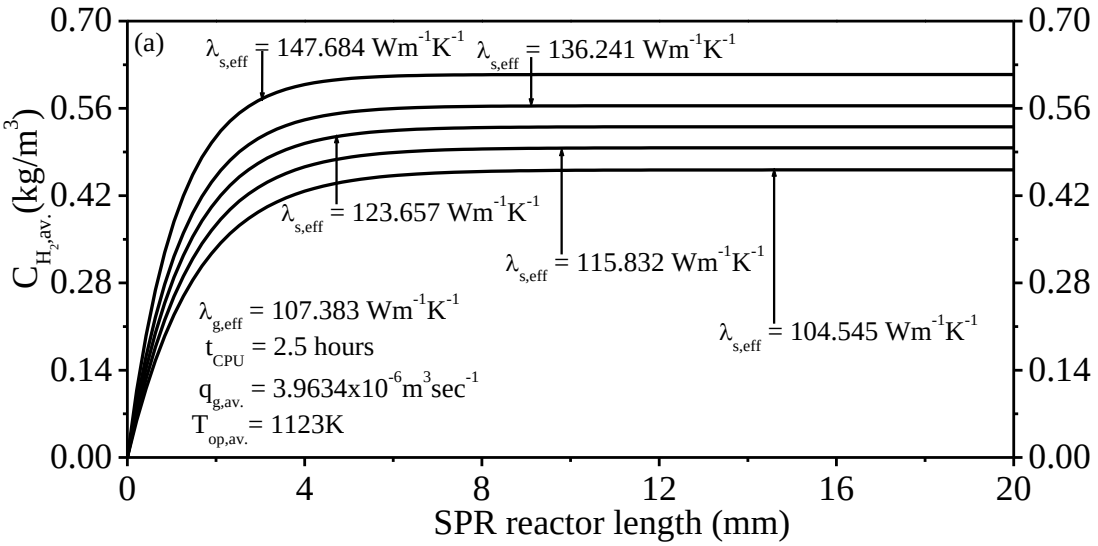

Figure 4. Effect of the $\lambda_{s,eff}$ on the production of H_2 using Ni/γ-Aℓ_2O_3) with 8% Ni loading.

Figure 5 reports the effect of the operating temperature on the overall conversion of reactants (CH_4 and CO_2) on the model reaction at operating condition of 650 kPa along the packed bed from SPR with radiative heat loss. Moreover, results of the overall conversion of reactants (CH_4 and CO_2) on the model reaction were computed at five different operating temperatures. From Fig. 3, the overall conversion of CH_4 is achieved to be at the center of outlet surface with the values of 0.6694 (T = 922K), 0.7701 (T = 973K), 0.8419 (T = 1023K), 0.9216 (T= 1073K), and 0.9895 (T =1123K), respectively. On the other hand, the conversion of CO_2 is a little lower than the conversion of CH_4 at the center of outlet surface. As it was shown in Figure 3, the overall conversion of CO_2 is reached to be at the center of outlet surface with the values of 0.4578 (T = 923K), 0.5401 (T = 973K), 0.5813 (T = 1023K), 0.6897 (T= 1073K), and 0.7789 (T = 1123K), respectively.

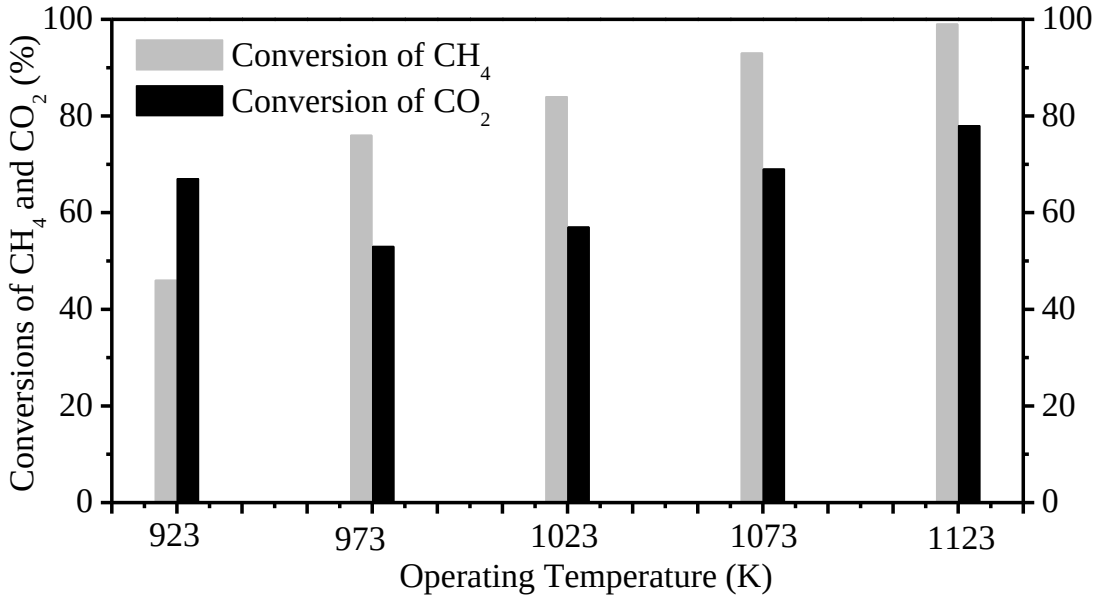

Figure 5. Conversions of CH_4 and CO_2 under different operating temperatures at the center of outlet surface from SPR.

5. CONCLUSION

The heat transfer and thermochemical performance of the SRT process are numerically investigated with radiative heat loss. A computer code to simulate and analyze the performance of the thermochemical process variables allowed the following conclusions:

1. The average temperature profile at the surface of the solid phase decreases from 2000K to more or less 1123K whereas the average temperature profile of the gas phase increases from 300K to more or less 1123K;
2. The average temperature profiles at the surface of the solid phase and the average temperature profiles of the gas phase are sharply affected by the DNI. As results, reaction temperature at the outlet surface region has varied of $1021.26 < T_{react.} < 1245.27$K.
3. The production of H_2 was remarkably increased with the increase of the $\lambda_{s,eff}$ at the outlet region from SPR;
4. The overall conversions of reactants of CH_4 and CO_2 reached values 98.95% and 77.89%, respectively, at the operating temperature of 1123K.

6. ACKNOWLEDGMENTS

The authors of this paper would like to thank the CNPQ (National Council for Scientific and Technological Development) for their financial support.

7. REFERENCES

Abdesslem, J., Khalifa, S., Abdelaziz, N. and Abdallah, M., 2013. "Radiative properties effects on unsteady natural convection inside a saturated porous medium. Application for porous heat exchangers". *Energy*, Vol. 61, pp. 224-233.

Anjos, E., Damasceno, J., Oliveira, C., Silva, A. and Silva, J., 2018. "Numerical Analysis of the steam reforming of toluene to produce hydrogen in a fixed bed catalytic reactor. In *Proceedings of the 17th Brazilian Congress of Thermal Sciences and Engineering – ENCIT 2018.* Águas de Lindoia - SP, Brazil.

Anjos, E., Oliveira, C. and Silva, J., 2019. "Dynamic analysis to produce hydrogen in a fixed bed catalytic reactor by the steam reforming of toluene." *Chemical Engineering Transaction*, Vol.74, pp. 553-558.

Anjos, E., Silva, J. and Damasceno, J., 2017. "Dynamic analysis of a three-phase reactor of fixed bed for petroleum and petrochemical Industry. In *Proceedings of the 24th ABCM International Congress of Mechanical Engineering – COBEM 2017*. Curitiba-PR, Brazil.

Chein, R. Y., Hsu, W. H. and Yu, C. T., 2017. "Parametric study of catalytic dry reforming of methane for syngas production at elevated pressures". *Int J Hydrogen Energy*, Vol. 42, pp. 14485-14500.

Chen, X., Wang, F., Yan X., Han, Y., Chen Z. and Jie Z., 2018. "Thermochemical performance of solar driven CO_2 reforming of methane in volumetric reactor with gradual foam structure". *Energy*, Vol. 151, pp. 545-555.

Cruz, B. M. and Silva, J. D., 2017. "A two-dimensional mathematical model for the catalytic steam reforming of methane in both conventional fixed-bed and fixed-bed membrane reactors for the Production of hydrogen. *Int J Hydrogen Energy*, Vol. 42, pp. 23670-23690.

Jin, J., Wei, X., Liu, M., Yu, Y., Li, W., Kong, H. and Hao, Y., 2018. "A solar methane reforming reactor design with enhanced efficiency". *Applied Energy*, Vol. 226, pp. 797-807.

Matienzo, J. M. R., 2018. "Influence of addition of hydrogen produced on board in the performance of a stationary diesel engine". *Int J Hydrogen Energy*, Vol. 43, pp. 17889-17897.

Silva, J. D. and Abreu, C. A. M., 2016. "Modelling and simulation in conventional fixed-bed and fixed-bed membrane reactors for the steam reforming of methane". *Int J Hydrogen Energy*, Vol. 41, pp. 11660-11674.

Silva, P. B. A., Carvalho, J. D. C. G., Silva, J. D., 2019. "Hydrogen adsorption on Ni/γ-$A\ell_2O_3$ in a fixed-bed adsorber: Experimental validation and numerical modelling". *Int J Hydrogen Energy*, Vol. 44, pp. 304-317.

Villafán-Vidales, H. I., Arancibia-Bulnes, C. A., Riveros-Rosas, D., Romero-Paredes, H., Estrada, C. A., 2017. "An overview of the solar thermochemical processes for hydrogen and syngas production: Reactors, and facilities". *Renewable and Sustainable Energy Reviews*, Vol. 75, pp. 894-908.

Annex A:

$$\alpha_{g,1}=\frac{L_z}{2}+\sum_{i=1}^{4}\rho_{g,i}\,C_{p,g,i}\,\frac{L_z^2}{3}\,\frac{q_g}{\pi\,d_\mu^2\,\lambda_{g,eff}\left(T_{g,0}\right)};\ \alpha_{g,2}=\sum_{i=1}^{4}\rho_{g,i}\,C_{p,g,i}\,\frac{L_z^2}{3}\,\frac{q_g}{\pi\,d_\mu^2\,\lambda_{g,eff}\left(T_{g,0}\right)} \tag{A1}$$

$$\alpha_{g,3}=\sum_{i=1}^{4}\rho_{g,i}\,C_{p,g,i}\,\frac{2L_z\,q_g}{\pi\,d_\mu^2\,\lambda_{g,eff}\left(T_{g,0}\right)};\ \alpha_{g,4}=\alpha_{g,1}+\frac{L_z}{2}\left(1+\alpha_{g,3}\right);\ \alpha_{g,5}=\frac{1+\alpha_{g,3}}{\alpha_{g,4}} \tag{A2}$$

$$\alpha_{g,6}=\frac{\alpha_{g,3}\left[\left(1+\alpha_{g,3}\right)-\alpha_{g,4}\right]}{\alpha_{g,4}};\ \alpha_{g,7}=\frac{4\,q_g}{\pi\,d_\mu^2}\left(\frac{2-\alpha_{g,4}\,\alpha_{g,5}}{\alpha_{g,4}}\right)-\frac{h_{gs}}{\sum_{i=1}^{4}\rho_{g,i}\,C_{p,g,i}}\,\frac{6}{d_p}\,\frac{\left(1-\varepsilon_b\right)}{\varepsilon_b} \tag{A3}$$

$$\alpha_{g,8}=\frac{h_{gs}}{\sum_{i=1}^{4}\rho_{g,i}\,C_{p,g,i}}\,\frac{6}{d_p}\,\frac{\left(1-\varepsilon_b\right)}{\varepsilon_b};\ \alpha_{g,9}=\frac{4\,q_g}{\pi\,d_\mu^2}\left(\frac{\alpha_{g,3}}{\alpha_{g,4}}-\alpha_{g,6}-1\right) \tag{A4}$$

Annex B:

$$\beta_{s,1}=\frac{h_{gs}}{\rho_s\,C_{p,s}}\,\frac{6}{d_p}\,\frac{\left(1-\varepsilon_b\right)}{\varepsilon_b};\ \beta_{s,2}=\frac{\varepsilon_w\,A_{cs}\,\sigma}{\rho_s\,C_{p,s}};\ \beta_{s,3}=\frac{\left(1-\varepsilon_b\right)}{\varepsilon_b\,C_{p,s}}\,\Delta H_1\,\eta_1;\ \beta_{s,4}=\frac{\lambda_{s,eff}\left(T_{g,0}\right)}{\rho_s\,C_{p,s}\,L_z^2\,\lambda_s\left(T_{g,0}\right)}\,DNI \tag{B1}$$

Annex C:

$$\gamma_1=L_z\left(\frac{1}{2}+\frac{L_z\,q_g}{3\pi\,d_\mu^2}\right);\ \gamma_2=\frac{L_z}{2}\left(1+\frac{L_z}{6}\,k_{g,i,eff.}\right);\ \gamma_3=\frac{L_z^2}{3}\left(\frac{q_g}{\pi\,d_\mu^2}\,C_{i,in.}-\frac{k_{g,i,eff.}}{6}\,C_\infty\right) \tag{C1}$$

$$\gamma_4=1+\frac{L_z}{2}\,k_{g,i,eff.};\ \gamma_5=1+\frac{2L_z\,q_g}{\pi\,d_\mu^2};\ \gamma_6=\frac{L_z}{2}\,k_{g,i,eff.}\,C_\infty-\frac{2\,L_z\,q_g}{\pi\,d_\mu^2}\,C_{i,in.};\ \gamma_7=\gamma_1+\frac{\gamma_2\,\gamma_5}{\gamma_4} \tag{C2}$$

$$\gamma_8=\gamma_3+\frac{\gamma_2\,\gamma_6}{\gamma_4};\ \gamma_9=\frac{\gamma_5}{\gamma_4\,\gamma_7};\ \gamma_{10}=\frac{1}{\gamma_4}\left(\frac{\gamma_5\,\gamma_8}{\gamma_7}-\gamma_6\right);\ \gamma_{11}=\frac{4\,q_g}{\varepsilon_b\,\pi\,d_\mu^2}+D_{ax,i}\,k_{g,i,eff.};\ \gamma_{12}=\frac{4\,q_g}{\pi\,d_\mu^2}\left(\frac{1}{\varepsilon_b}-D_{ax,i}\right) \tag{C3}$$

$$\gamma_{13}=D_{ax,i}\left(k_{g,i,eff.}\,C_\infty+\frac{4\,q_g}{\pi\,d_\mu^2}\,C_{i,in.}\right);\ \gamma_{14}=\frac{\gamma_{12}}{\gamma_7}-\gamma_{11}\,\gamma_9;\ \gamma_{15}=\gamma_{11}\left(\frac{\gamma_8}{\gamma_7}-\gamma_{10}\right)+\gamma_{13} \tag{C4}$$

8. RESPONSIBILITY NOTICE

The authors are the only responsible for the printed material included in this paper.